PHYSICS

Interface-engineered electron and hole tunneling

Rui Guo[1,2]*, Lingling Tao[3]*, Ming Li[3], Zhongran Liu[4], Weinan Lin[1], Guowei Zhou[1,5], Xiaoxin Chen[4], Liang Liu[1], Xiaobing Yan[2], He Tian[4†], Evgeny Y. Tsymbal[3†], Jingsheng Chen[1†]

Although the phenomenon of tunneling has been known since the advent of quantum mechanics, it continues to enrich our understanding of many fields of science. Commonly, this effect is described in terms of electrons traversing the potential barrier that exceeds their kinetic energy due to the wave nature of electrons. This picture of electron tunneling fails, however, for tunnel junctions, where the Fermi energy lies sufficiently close to the insulator valence band, in which case, hole tunneling dominates. We demonstrate the deterministic control of electron and hole tunneling in interface-engineered Pt/$BaTiO_3$/$La_{0.7}Sr_{0.3}MnO_3$ ferroelectric tunnel junctions by reversal of tunneling electroresistance. Our electrical measurements, electron microscopy and spectroscopy characterization, and theoretical modeling unambiguously point out to electron or hole tunneling regimes depending on interface termination. The interface control of the tunneling regime offers designed functionalities of electronic devices.

INTRODUCTION

Electron tunneling is a quantum-mechanical effect, where electrons traverse the potential barrier that exceeds their kinetic energy, reflecting the wave nature of electrons (*1*). Numerous useful electronic devices are based on this phenomenon. For example, electron tunneling is exploited in superconducting quantum interference devices (SQUIDs) based on Josephson junctions (*2*). Electron tunneling is the basic principle of scanning tunneling microscopy (*3*). The Fowler-Nordheim tunneling (*4*) is used in flash memories and field emission displays. Electron tunneling controls properties of magnetic tunnel junctions (*5*–*7*), key elements in magnetic random access memories, and ferroelectric tunnel junctions (FTJs) (*8*–*11*), which have the potential to overperform conventional random access memories based on ferroelectric capacitors (*12*–*15*).

A common picture of quantum-mechanical tunneling assumes that with increasing electron energy, the effective potential barrier height decreases, resulting in a slower decay of an electron wave (*16*). For example, if U is the potential barrier height and E_F is the Fermi energy, the decay constant is given by $\kappa_e^2 = 2m_e(U - E_F)/\hbar^2$, where m_e is the electron mass. This picture silently assumes that E_F is located sufficiently close to the conduction band minimum (CBM) of the insulator, so that electron tunneling controls transmission, and the potential barrier height is determined by the CBM energy, i.e., $U = E_{CBM}$ (fig. S1A). However, if E_F is located sufficiently close to the valence band maximum (VBM) of the insulator, the decay constant is given by $\kappa_h^2 = -2m_h(U - E_F)/\hbar^2$, where m_h is the hole mass and the potential barrier height is determined by the VBM energy, i.e., $U = E_{VBM}$ (fig. S1B). In this case of hole tunneling, the effective potential barrier height increases with increasing E_F, resulting in a higher decay constant. The crossover between the two tunneling regimes is determined by the decay constant κ, which depends on energy. Figure 1A schematically shows variation of κ within the insulator bandgap. Depending on E_F, either electron or hole tunneling controls transport properties. The two regimes are distinguished by the κ dependence on energy E: While for electron tunneling, κ decreases with increasing E, for hole tunneling, κ increases with increasing E. The decay rate is determined by the evanescent states in

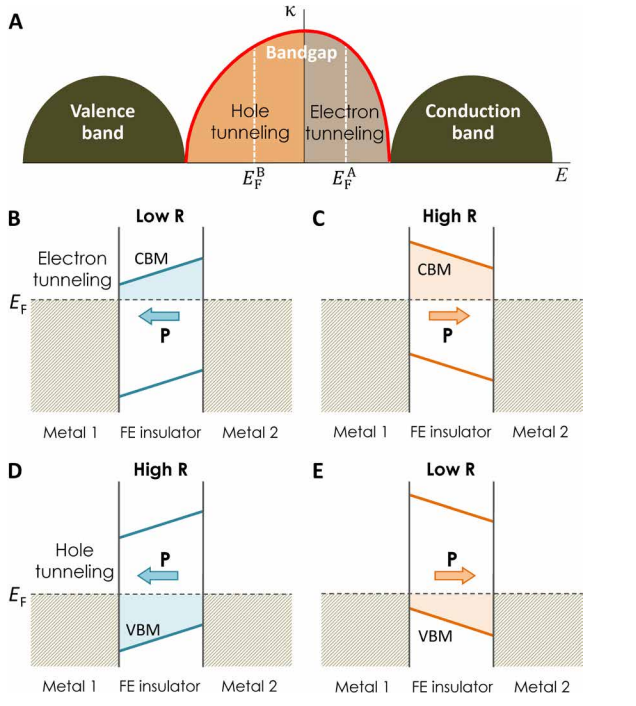

Fig. 1. Crossover between electron and hole tunneling and its role in an FTJ. (**A**) Decay constant κ (red line) versus energy E. Electron and hole tunneling regimes are distinguished by the Fermi energy (dashed lines) in the bandgap of the insulator. (**B** to **E**) Schematic of the TER effect. For electron tunneling, resistance is low (B) when polarization (shown by arrow) is pointing from metal 2 with a shorter screening length to metal 1 with a longer screening length, and resistance is high (C) for reversed polarization. For hole tunneling, the effect is opposite: Resistance is high (D) for polarization pointing from metal 1 to metal 2, and resistance is low (E) for reversed polarization. FE stands for ferroelectric.

[1]Department of Materials Science and Engineering, National University of Singapore, 117575 Singapore, Singapore. [2]College of Electron and Information Engineering, Hebei University, Baoding 071002, China. [3]Department of Physics and Astronomy and Nebraska Center for Materials and Nanoscience, University of Nebraska, Lincoln, NE 68588-0299, USA. [4]Center of Electron Microscope, State Key Laboratory of Silicon Materials, School of Materials Science and Engineering, Zhejiang University, Hangzhou 310027, China. [5]Key Laboratory of Magnetic Molecules and Magnetic Information Materials of Ministry of Education, School of Chemistry and Materials Science, Shanxi Normal University, Linfen 041004, China.
*These authors contributed equally to this work.
†Corresponding author. Email: msecj@nus.edu.sg (J.C.); tsymbal@unl.edu (E.Y.T.); hetian@zju.edu.cn (H.T.)

the energy gap region of the insulator (*17*), which control both electron and hole tunneling.

FTJs provide a unique opportunity to explore and control electron or hole tunneling. An FTJ consists of two metal electrodes separated by a nanometer-thick ferroelectric barrier layer (*8*). The key property of FTJ is tunneling electroresistance (TER), i.e., a resistance change with reversal of ferroelectric polarization. There are several mechanisms responsible for TER (*18*–*25*). The most common involves modulation of the effective potential barrier height (*18*). FTJ resistance is low when polarization is pointing from the electrode with a shorter screening length to the electrode with a longer screening length (Fig. 1B) and is high for the reversed polarization (Fig. 1C). This picture assumes that tunneling conduction is governed by electrons, which occurs if E_F lies sufficiently close to the CBM. For the hole tunneling, however, the situation is opposite. In this case, the tunneling barrier is determined by the VBM proximity. The effective barrier and thus FTJ resistance are high when polarization is pointing from the electrode with a longer screening length to the electrode with a shorter screening length (Fig. 1D) and are low for the reversed polarization (Fig. 1E). Thus, TER is indicative to the tunneling regime and is opposite for electron and hole tunneling.

RESULTS

In this work, we report observation of switching between electron and hole tunneling in FTJs with different interface terminations. We fabricate FTJs with top Pt and bottom ($La_{0.7}Sr_{0.3}MnO_3$) LSMO electrodes and $BaTiO_3$ (BTO) ferroelectric barrier. The bottom BTO/LSMO interface has either $TiO_2/La_{0.7}Sr_{0.3}O$ (A-type FTJ) or BaO/MnO_2 (B-type FTJ) termination, as schematically shown in Fig. 2 (A and B). We use chemically treated (001) $SrTiO_3$ (STO) substrates to obtain either a SrO-terminated (A-type) surface or a

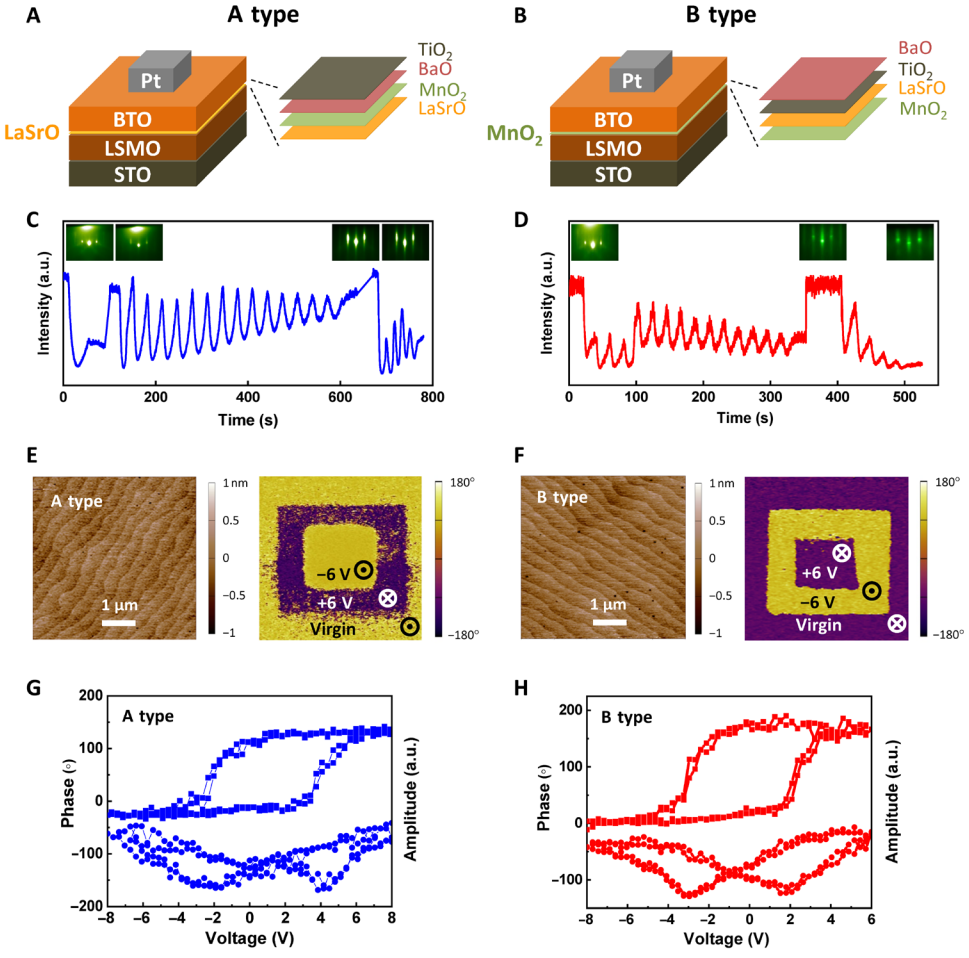

Fig. 2. RHEED and scanning probe microscopy characterization of A- and B-type FTJs. (**A** and **B**) Schematic of A-type (A) and B-type (B) FTJs. The atomic plane sequences across the BTO/LSMO interfaces are indicated. In the notation, LaSrO stands for $La_{0.7}Sr_{0.3}O$. (**C**) RHEED intensity oscillations of the specular reflected beam during the growth of 1 u.c. of SRO layer on the TiO_2-terminated STO substrate to obtain the SrO termination and the subsequent growth of the 15-u.c. LSMO and then 5-u.c. BTO thin films on top of it. a.u., arbitrary units. (**D**) RHEED intensity oscillations of the specular reflected beam during the growth of the 15-u.c. LSMO thin film on the TiO_2-terminated STO substrate and the following growth of the 5-u.c. BTO thin film. The insets show the RHEED patterns before and after each thin-film layer growth. (**E** and **F**) Atomic force microscopy topography (left) and out-of-plane PFM phase images (right) of the BTO thin films in A-type (E) and B-type (F) BTO/LSMO/STO heterostructures measured directly on the BTO films after the film deposition. The yellow and purple contrasts in the PFM phase images represent the upward and downward polarization direction, respectively. (**G** and **H**) Typical local PFM amplitude (circles) and phase (squares) hysteresis loops of BTO thin films for A-type (G) and B-type (H) Pt/BTO/LSMO FTJs measured on top Pt electrodes.

TiO_2-terminated (B-type) surface of STO (see Materials and Methods for details). Then, the LSMO bottom electrode and 5-unit-cell (u.c.) BTO barrier layer are epitaxially grown using pulsed laser deposition (PLD). Film thickness is controlled by reflection high-energy electron diffraction (RHEED), demonstrating a unit cell–by–unit cell thin-film growth mode (Fig. 2, C and D). Such epitaxial growth maintains the perovskite stacking sequence across LSMO/STO and BTO/LSMO interfaces resulting in $TiO_2/La_{0.7}Sr_{0.3}O$- or BaO/MnO_2-terminated BTO/LSMO interfaces for FTJs on SrO- or TiO_2-terminated STO substrates, respectively. After the PLD deposition, the top Pt layer is deposited by magnetron sputtering without breaking vacuum.

The resulting A- and B-type FTJs have polar BTO/LSMO interfaces with opposite sign of ionic charges. While (001) BTO is composed of charge neutral $(BaO)^0$ and $(TiO_2)^0$ atomic layers, (001) LSMO consists of charged $(La_{0.7}Sr_{0.3}O)^{+0.7}$ and $(MnO_2)^{-0.7}$ layers. This implies that the (001) BTO/LSMO interface is polar: The $(TiO_2)^0/(La_{0.7}Sr_{0.3}O)^{+0.7}$-terminated interface has a positive bound charge of $+0.35e$ per lateral unit cell area, whereas the $(BaO)^0/(MnO_2)^{-0.7}$-terminated interface has a negative bound charge of $-0.35e$. Despite LSMO being a metal, these interfacial ionic charges are not fully screened, resulting in the notable changes in the electronic and magnetic properties of the interfaces, as well documented in the literature (*26*–*30*).

The presence of polar interfaces affects ferroelectric behavior of BTO films. Our piezoresponse force microscopy (PFM) measurements show that polarization direction of as-grown BTO films is opposite for A- and B-type interfaces (Fig. 2, E and F). While in a virgin state, the positively charged $(TiO_2)^0/(La_{0.7}Sr_{0.3}O)^{+0.7}$ interface favors polarization pointing away from the interface (yellow color contrast in Fig. 2E), the negatively charged $(BaO)^0/(MnO_2)^{-0.7}$ interface favors polarization pointing into it (purple color contrast in Fig. 2F). After applying a bias of −6 or +6 V, the virgin upward or downward BTO polarization is switched to the opposite direction, and then, it is switched back to its original direction when an opposite bias is applied. Figure 2 (G and H) shows typical local PFM amplitude and phase hysteresis loops of BTO thin films covered by the Pt layer and measured across this layer. These results demonstrate a standard local hysteretic electromechanical response, indicating switchable polarization of the BTO layer in the presence of the top Pt electrode. It is notable that for both A- and B-type FTJs, the hysteresis loops exhibit a sizable imprint, indicating the presence of a built-in electric field across the BTO layer. This electric field has an opposite sign for the A- and B-type FTJs, consistent with the polarity of the respective interfaces.

To investigate transport properties, we carried out electrical measurements (see Materials and Methods for details). Figure 3 (A and B) shows the *I-V* (current-voltage) curves in the low-bias regime, from −0.3 to +0.3 V, after the BTO polarization has been saturated downward or upward by applying positive (+6 V) or negative (−6 V) voltage. The same polarization orientation results in opposite resistance states for the two types of FTJs: The downward (upward) polarization exhibits low (high) and high (low) resistance states for A- and B-type FTJs, respectively. This indicates that changing the interface termination from A to B type leads to the reversal of TER.

Consistent with these results, *I-V* characteristics in a broader voltage range, from −7 to +7 V, reveal opposite resistive switching behavior (Fig. 3, C and D). For the A-type FTJ, sweeping voltage from negative to positive produces a low-current curve, whereas sweeping voltage from positive to negative produces a high-current curve (Fig. 3C). On the contrary, for the B-type FTJ, sweeping voltage from negative to positive produces a high-current curve, whereas sweeping voltage from positive to negative produces a low-current curve (Fig. 3D).

This behavior is further corroborated by measured resistance loops shown in Fig. 3 (E and F). Here, FTJ resistance is read out at +0.2 V bias after applying a writing voltage pulse. With a negative voltage pulse, BTO is poled upward, and A-type FTJ is set to a high-resistance OFF state (Fig. 3E), whereas B-type FTJ is set to a low-resistance ON state (Fig. 3F). Changing voltage pulse polarity reverses polarization of BTO and switches the resistance states. Sweeping voltage from negative to positive and back produces hysteresis loops, which exhibit reversed resistive switching behaviors for the two types of FTJs. The electrical measurements on different Pt/BTO/LSMO samples confirm the TER reversal independent of LSMO (figs. S3 and S4) and BTO (fig. S5) layer thicknesses.

Scanning transmission electron microscopy (STEM) and electron energy-loss spectroscopy (EELS) characterization provides further insights into structural and electronic properties of FTJs. Figure 4 (A and B) shows the typical cross-sectional STEM images and atomic-resolution energy-dispersive x-ray (EDX) elemental maps of A- and B-type heterostructures. These data clearly reveal the TiO_2/LaSrO and BaO/MnO_2 interface terminations for A- and B-type FTJs, respectively (see also fig. S6). Displacement of Ti ions (insets in Fig. 4, A and B) indicates the upward and downward polarization of A- and B-type FTJs, respectively. The opposite polarization directions of as-grown BTO films revealed by STEM are consistent with our PFM results shown in Fig. 2 (E and F).

Figure 4 (C and D) shows the atomically resolved layer-by-layer EELS data, which allows us to analyze the band alignment across the BTO/LSMO interface. The position of the Fermi level E_F with respect to the VBM of BTO is determined by the valence band offset (VBO), as follows (*31*): $VBO = (VBM - E_{Ti\text{-}L3})_{BTO} + (E_{Ti\text{-}L3} - E_{Mn\text{-}L3})_{BTO/LSMO} + (E_{Mn\text{-}L3} - E_F)_{LSMO}$. The VBOs are different for the A- and B-type junction heterostructures, and their difference is $VBO_A - VBO_B = (E_{Ti\text{-}L3} - E_{Mn\text{-}L3})_A - (E_{Ti\text{-}L3} - E_{Mn\text{-}L3})_B$. From the EELS data, we obtain the following: $(E_{Ti\text{-}L3})_A = 469.6$ eV, $(E_{Mn\text{-}L3})_A = 650.6$ eV, $(E_{Ti\text{-}L3})_B = 468.3$ eV, and $(E_{Mn\text{-}L3})_B = 651.7$ eV (dashed lines in Fig. 4, C and D), resulting in $VBO_A - VBO_B = 2.4$ eV. Thus, our EELS data reveal that the VBO is 2.4 eV larger for the A-type heterostructure than for the B-type heterostructure. This implies E_F being closer to CBM (VBM) for the A-type (B-type) FTJ, as schematically illustrated in fig. S7.

This behavior is consistent with the interfacial ionic charges. The positively charged $(TiO_2)^0/(La_{0.7}Sr_{0.3}O)^{+0.7}$ interface (A-type) pulls the electrostatic potential energy down and shifts E_F closer to CBM. In contrast, the negatively charged $(BaO)^0/(MnO_2)^{-0.7}$ interface (B-type) pulls the energy up and shifts E_F closer to VBM. This fact is confirmed by our band structure calculations for a BTO/LSMO superlattice with A- and B-type interface terminations (see Materials and Methods for details). In these calculations, we assume that top and bottom BTO/LSMO interfaces are chemically identical, either $TiO_2/La_{0.7}Sr_{0.3}O$ (Fig. 5A, right) or BaO/MnO_2 (Fig. 5B, right). As a result, for a given polarization orientation (directing down in Fig. 5, A and B), this structural model allows us to determine band alignments between BTO and LSMO for polarization pointing to the interface (bottom interface) and away from the interface (top interface). Figure 5 (A and B) shows the calculated

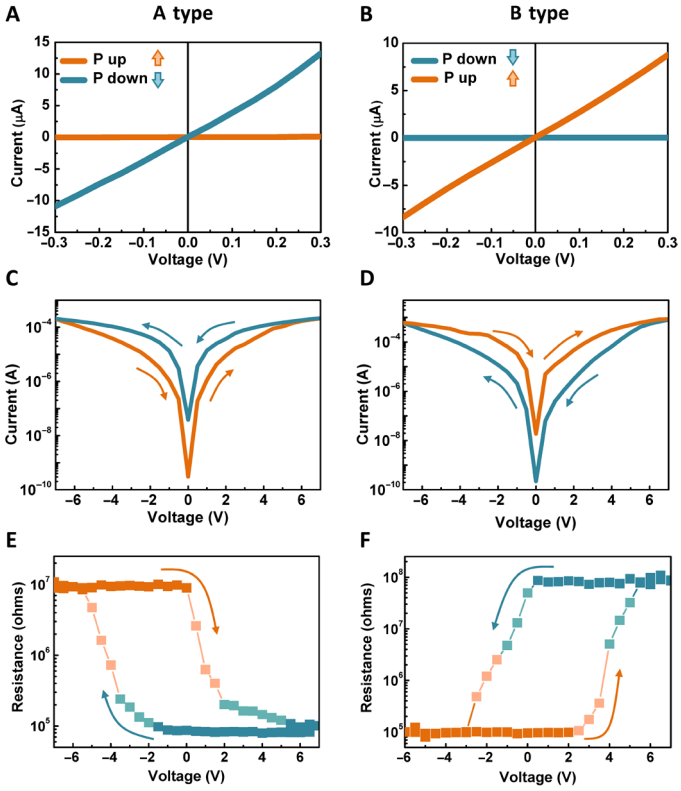

Fig. 3. Transport properties of Pt/BTO (5 u.c.)/LSMO (15 u.c.) FTJs with different interface terminations. (**A** and **B**) Typical *I-V* curves within a small voltage range for A-type (A) and B-type (B) FTJs. The *I-V* curves are measured after poling the BTO layer upward (downward) using a voltage bias pulse of −6 V (+6 V) and duration of 1 ms. (**C** and **D**) Typical *I-V* switching curves for A-type (C) and B-type (D) FTJs. Absolute values of the current are used to plot the data in the logarithmic scale. (**E** and **F**) Representative *R-V* hysteresis loops for A-type (E) and B-type (F) FTJs.

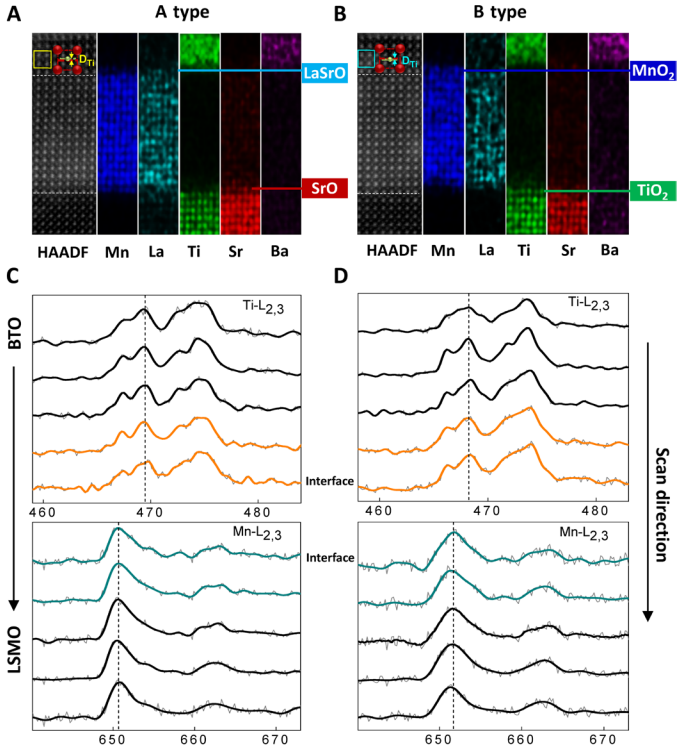

Fig. 4. STEM results for BTO/LSMO/STO heterostructures with different interface terminations. (**A** and **B**) High-angle annular dark-field (HAADF) images and EDX elemental maps of A-type (A) and B-type (B) heterostructures. The insets show the off-center displacement of Ti ions in the BTO layer. (**C** and **D**) Layer-resolved EELS spectra of Ti-$L_{2,3}$ and Mn-$L_{2,3}$ edges for A-type (C) and B-type (D) heterostructures. Arrows indicate the scan direction. Dashed lines mark the Ti-L_3 and Mn-L_3 peak positions.

layer-projected density of states (DOS) across the BTO layer. For the A-type interface, E_F lies close to the CBM, particularly near the bottom of BTO (Fig. 5A). On the contrary, for the B-type interface, E_F is shifted down closer to the VBM of BTO (Fig. 5B), which is qualitatively consistent with our EELS data.

Including Pt layer in the computational model adds more complexity due to different work functions of LSMO and Pt but does not change this conclusion (fig. S8). The higher work function of Pt is reflected in a built-in electric field pointing from LSMO to Pt across the BTO layer. Nevertheless, even in the presence of this field, E_F is shifted deeper from the CBM into the BTO bandgap for B-type termination (fig. S8B) than for A-type termination (fig. S8A).

The band alignment affects the quantum-mechanical tunneling regime, which can be understood in terms of evanescent states (*17*) and the complex band structure (*32*, *33*). Figure 5C shows the calculated imaginary part κ of the complex wave vector for several bands of BTO along the Γ-*Z* direction in the Brillouin zone. Evanescent bands with the lowest κ (denoted Δ_1 and Δ_5 by their symmetry) have the slowest decay rates and thus dominate in conductance. Changing energy E leads to an increase or decrease of κ, depending on E_F. In the energy window from $E \approx 2.3$ eV to $E \approx 3.2$ eV (CBM), the decay rates of the Δ_1 and Δ_5 states decrease with increasing E, which is typical to electron tunneling (gray area in Fig. 5C). On the contrary, in the energy window from $E = 0$ eV (VBM) to $E \approx 2.3$ eV, the decay rate of the Δ_1 state increases with increasing E, which is typical to hole tunneling (orange area in Fig. 5C). At $E \approx 2.3$ eV, there is a crossover between electron and hole tunneling. Including all evanescent states in the computation model (see Materials and Methods for details) alters the crossover point to $E \approx 1.5$ eV but does not qualitatively change the main result (Fig. 5D). This picture of tunneling elaborates the qualitative description of Fig. 1A.

DISCUSSION

With all this information in place, we can conclude that reversal of TER in Pt/BTO/LSMO FTJs, from normal for A-type FTJs to inverse for B-type FTJs, originates from crossover between the electron and hole tunneling regimes due to different interface terminations. Depending on the polarity of the BTO/LSMO interface—positive for the A-type FTJ and negative for the B-type FTJ—the Fermi level is located closer to the CBM or VBM of the BTO layer, respectively. The different position of the Fermi level in the two types of FTJs leads to opposite energy dependence of the transmission probability as a function of energy, designating electron and hole tunneling.

Overall, our results demonstrate an important fundamental feature in the long-studied phenomenon of quantum-mechanical tunneling. The concept of a hole has been well known in semiconductor physics and has been heavily exploited to describe transport properties of semiconductors and devices using them. In semiconductors, a hole is simply an electron vacancy in the valence band. Like an

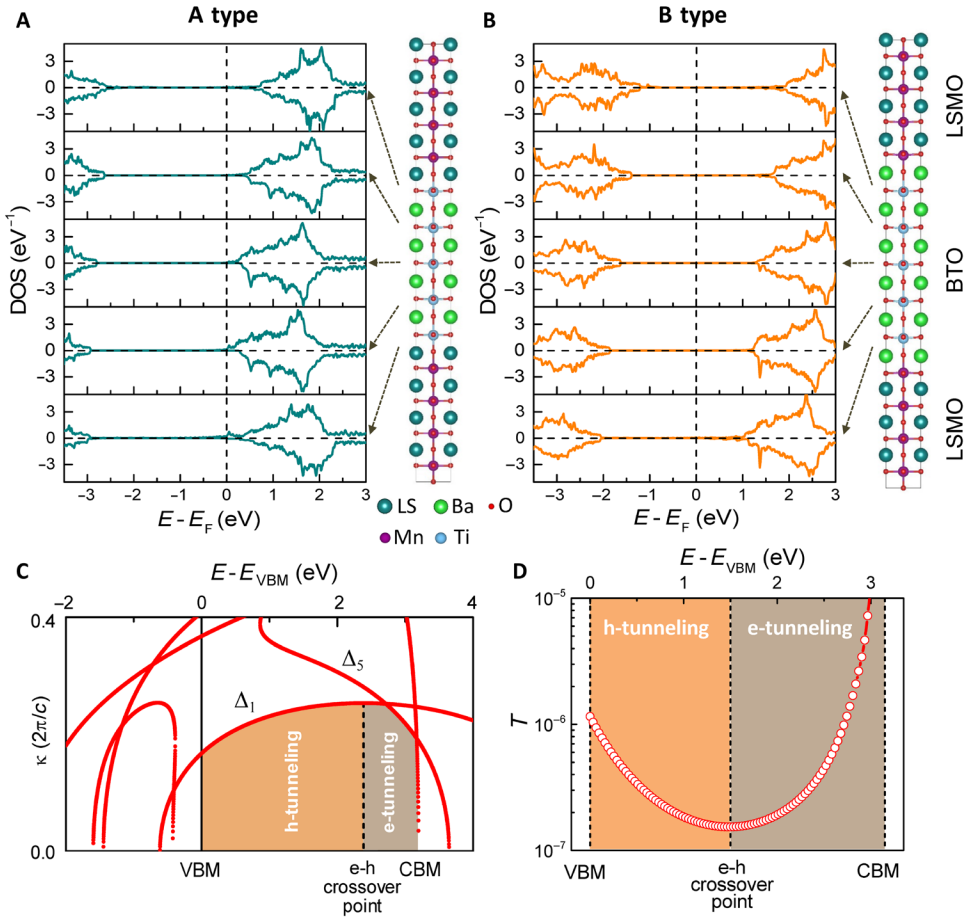

Fig. 5. Calculated electronic structure of LSMO/BTO superlattice and evanescent states in BTO. (**A** and **B**) Local density of states (DOS) across the BTO layer for (A) $TiO_2/La0.7Sr_{0.3}O$ (A-type) and (B) BaO/MnO_2 (B-type) terminations. Positive and negative DOS correspond to up- and down-spin contributions. Dashed lines indicate the Fermi energy. Ferroelectric polarization of BTO is assumed to be pointing down. Right panels in (A) and (B) show the LSMO/BTO supercells used in the calculations. (**C**) Calculated decay constant κ at the $\bar{\Gamma}$ point ($\mathbf{k}_{\parallel} = 0$) as a function of energy. Evanescent bands of Δ_1 and Δ_5 symmetry are indicated. (**D**) Calculated transmission across the 5-u.c.-thick BTO layer.

electron, it can be moved under an applied electric field carrying charge. In case of an insulator representing a tunnel barrier where the valence band is fully occupied, hole transport has a somewhat different meaning. Instead of a moving electron vacancy in the valence band, the proximity of the latter to the Fermi energy determines the tunneling potential barrier. The height of this barrier is enhanced with increasing the carrier energy, which is opposite to what is expected from the standard picture of electron tunneling and designates hole tunneling.

Recent advances in thin-film deposition and characterization techniques make possible fabrication of oxide heterostructures with atomic-scale precision and allow continuous variation of the interface stoichiometry (*34*, *35*). Such interface engineering permits switching of the transport regime between electron and hole tunneling, which controls conductance of the tunnel junction and the TER sign and magnitude. Because of the different energy dependence of the transmission coefficient in these regimes, differential resistance of a tunnel junction can be adjusted to a value appropriate for device applications. This functionality may be useful to implement solid-state synapses for neuromorphic computing (*36*–*38*), develop novel photovoltaic (*39*) and van der Waals FTJs (*40*, *41*), and control spin-dependent transport by ferroelectric polarization (*42*–*46*).

MATERIALS AND METHODS

Device fabrication

LSMO thin films with different thicknesses were epitaxially grown on (001) single-crystalline STO substrates as the bottom electrodes by PLD using a KrF (λ = 248 nm) excimer laser, followed by the deposition of ultrathin BTO (5 u.c.) as the barrier layer. LSMO thin films were grown at a substrate temperature of 750°C with an oxygen pressure of 200 mtorr, while BTO films were deposited at a substrate temperature of 600°C with an oxygen partial pressure of 5 mtorr. All thin films were deposited using the unit cell–by–unit cell growth mode monitored by RHEED oscillations (Fig. 2, C and D). STO substrates were treated before the deposition. To get a TiO_2-terminated surface, a buffered hydrofluoric acid etching process was done followed by a thermal treatment at 950°C for 3 hours. The SrO-terminated surface was obtained by growing 1 u.c. of SRO layer on top of treated TiO_2-terminated STO substrates using $SrRuO_3$ target. The 1-u.c. $SrRuO_3$ layer was deposited at a substrate temperature of 750°C and an oxygen pressure of 10 mtorr. At the high temperature, RuO_2 monolayer evaporated, leaving the SrO-terminated surface automatically. After the deposition, the films were cooled down to room temperature at an oxygen pressure of 200 torr, with the cooling rate of 5°C/min until 300°C and then 10°C/min to room

temperature. Then, the top Pt layer is deposited by magnetron sputtering without breaking vacuum by transferring the sample directly from PLD chamber to sputtering chamber. Following this, an array of 10 μm–by–10 μm top Pt electrodes is patterned via photolithography and etching for electrical measurements.

STEM measurements

Microstructure of the two types of FTJs, interfacial structure, EDX elemental mapping, and atomic layer by layer EELS were conducted by aberration-corrected STEM at room temperature. Cross-sectional STEM samples were prepared with a focused ion beam setup (DA300, FEI). The microstructure of the FTJ was characterized using aberration-corrected STEM at high-angle annular dark-field mode. Element distribution of the films was tested using EDX mapping on an FEI Titan G2 80-200 microscope equipped with a Super-X EDX detector at an emission voltage of 200 kV.

PFM measurements

The ferroelectric polarization and the local hysteresis loop of as-grown ultrathin BTO films were characterized using piezoelectric force microscopy (PFM) (Asylum Research MFP-3D) with Pt/Ti-coated tips. Topography and PFM phase images were measured directly on top of BTO films. The measurement was performed under contact mode with an AC voltage applied to the probe tip using a scan rate of 0.5 μm/s. PFM local hysteresis loops of two types of FTJs were measured on top of Pt electrodes.

Electrical measurements

The measurements of the transport properties of FTJs were carried out using the two-point measurement method in a low-noise probe station. The *I*-*V* and *R*-*V* (resistance-voltage) curves were measured using a pA meter/dc voltage source (Hewlett-Packard 4140B). The applied voltage is termed as positive (negative) if a positive (negative) bias is applied to the top Pt electrode. *I*-*V* curves within a small voltage range are measured after poling the BTO polarization upward or downward. *I*-*V* switching curves are measured by sweeping the voltage from −7 to +7 V and then back to −7 V. *R*-*V* curves are performed by measuring current at a bias voltage of +0.2 V after applying voltage pulses of different magnitude and sign, and duration of 1 ms.

To verify the tunneling nature of the electric conduction in our FTJs, temperature- and time-dependent transport properties are measured. The results shown in fig. S2 clearly indicate that the steady-current tunneling characteristics are different from thermally activated or transient charge-injection events. In addition, we find that the *I*-*V* curves can be well fitted by the direct tunneling theory based on the Wentzel-Kramers-Brillouin (WKB) approximation (see the "Fitting *I*-*V* characteristics" section below for details), which further confirms the tunneling origin of the measured conductance (fig. S3).

Theoretical modeling

Density functional theory (DFT) calculations were performed using a plane-wave pseudopotential method within a generalized gradient approximation for the exchange-correlation functional, as implemented in Quantum-ESPRESSO (*47*). The BTO/LSMO heterostructure was modeled by a superlattice consisting of 8.5-u.c. LSMO and 4.5-u.c. BTO for the $La_{0.7}Sr_{0.3}O$-terminated interface and 7.5-u.c. LSMO and 5.5-u.c. BTO for the MnO_2-terminated interface, as shown in Fig. 5 (A and B, right).

We note that using symmetrically terminated interfaces (either A- or B-type) allows us to avoid potential variation across the BTO layer associated with different interface bound charges. This simplifies quantifying the band offset between LSMO and BTO in the presence of ferroelectric polarization. The presence of symmetric interfaces and thus nonstoichiometric LSMO produces an effect of doping. However, this doping is confined to the interfaces due to the interface charge being screened within a couple of unit cells from LSMO interfaces. As a result, there is no doping of bulk LSMO, and thus, the band alignment is only controlled by the interface termination.

The Pt/BTO/LSMO heterostructures were modeled using a superlattice consisting of 5-u.c. LSMO, 4-u.c. Pt, and 5-u.c. BTO for the $La_{0.7}Sr_{0.3}O$-terminated interface and 4.5-u.c. LSMO, 4-u.c. Pt, and 5.5-u.c. BTO for the MnO_2-terminated interface. The Pt/BTO interface was considered to be Pt/BaO, while the Pt/LSMO interface was assumed to be Pt/MnO_2.

In the calculations, a plane-wave energy cutoff was set equal to 544 eV. The La-Sr substitutional disorder was treated using a virtual crystal approximation, which has been found to correctly reproduce the electronic and magnetic properties of LSMO in the metallic phase (*48*). To simulate epitaxial growth on an STO substrate, the in-plane lattice constant was constrained to the calculated value for bulk STO, a = 3.931 Å. Under such a constraint, both bulk LSMO and BTO are found to be tetragonal with c/a = 0.977 for LSMO and c/a = 1.053 for BTO. For the BTO/LSMO heterostructure, both the out-of-plane lattice constant and all internal atomic coordinates were fully relaxed with the force tolerance of 26 meV/Å. A 6 × 6 × 1 k-point mesh was used for structural relaxation calculation. The subsequent self-consistent calculation was performed with a 10 × 10 × 1 k-point mesh and U = 8 eV for the Ti-3d orbital to match the calculated bandgap of BTO to the experimental bandgap.

The complex band structure for bulk BTO was calculated using a tight-binding Hamiltonian obtained from the Wannier interpolation approach implemented in the Wannier90 code (*49*). Transmission shown in Fig. 5D was obtained within a simple approximation assuming that $T \propto \sum_{n\mathbf{k}_\parallel} e^{-2\kappa_n(\mathbf{k}_\parallel)t}$, where $\kappa_n(\mathbf{k}_\parallel)$ is the decay constant on the nth evanescent state at the transverse wave vector $\mathbf{k}_\parallel$ and t is the BTO layer thickness. In the calculation, summation over 100 × 100 $\mathbf{k}_\parallel$ points in the two-dimensional Brillouin zone was performed, and the BTO layer thickness was assumed to be 5 u.c., i.e., t = 2.1 nm.

Fitting *I*-*V* characteristics

Fitting of the measured *I*-*V* curves was performed using the direct tunneling theory based on the WKB approximation, according to which the current density J as a function of voltage V is given in (*50*)

$$J(V) = C\frac{\mathrm{Exp}\left\{\alpha(V)\left[\left(\Phi_2 - \frac{\mathrm{eV}}{2}\right)^{\frac{3}{2}} - \left(\Phi_1 + \frac{\mathrm{eV}}{2}\right)^{\frac{3}{2}}\right]\right\}}{\alpha^2(V)\left(\sqrt{\Phi_2 - \frac{\mathrm{eV}}{2}} - \sqrt{\Phi_1 + \frac{\mathrm{eV}}{2}}\right)} \times \sinh\left[\frac{3\ \mathrm{eV}}{4}\alpha(V)\left(\sqrt{\Phi_2 - \frac{\mathrm{eV}}{2}} - \sqrt{\Phi_1 + \frac{\mathrm{eV}}{2}}\right)\right] \quad (1)$$

where $C = (4em^*)/(9\pi^2\hbar^3)$, m^* is the effective mass of carriers, $\alpha(V) = 4d\sqrt{2m^*}/[3\hbar(\Phi_1 - \Phi_2 + \mathrm{eV})]$, d is the tunnel barrier (BTO)

width, and $\Phi_{1,2}$ represent the tunneling barrier heights at the two interfaces. The results of the fitting are shown in fig. S3 (A and B), and the fitted parameters are listed in table S1. We note that while the barrier heights are similar for FTJs with 15- and 50-u.c. LSMO layers, they somewhat deviate for the 8-u.c. LSMO FTJ. The latter is likely caused by the enhanced resistance of the LSMO layer, which is not taken into account by the fitting. Figure S9 (A and B) schematically shows the polarization-dependent potential barriers obtained from the fitting results for FTJs with a 15-u.c. LSMO layer. These potential barriers are in remarkable agreement with those obtained from our DFT calculations for Pt/LSMO/BTO FTJs shown in fig. S9 (C and D).

SUPPLEMENTARY MATERIALS

Supplementary material for this article is available at http://advances.sciencemag.org/cgi/content/full/7/13/eabf1033/DC1

REFERENCES AND NOTES

1. J. Frenkel, On the electrical resistance of contacts between solid conductors. *Phys. Rev.* **36**, 1604–1618 (1930).
2. B. D. Josephson, The discovery of tunnelling supercurrents. *Rev. Mod. Phys.* **46**, 251–254 (1974).
3. G. Binnig, H. Rohrer, Scanning tunneling microscopy—From birth to adolescence. *Rev. Mod. Phys.* **59**, 615–625 (1987).
4. R. G. Forbes, J. H. B. Deane, Reformulation of the standard theory of Fowler–Nordheim tunnelling and cold field electron emission. *Proc. R. Soc. A* **463**, 2907–2927 (2007).
5. E. Y. Tsymbal, O. N. Mryasov, P. R. LeClair, Spin-dependent tunnelling in magnetic tunnel junctions. *J. Phys. Condens. Matt.* **15**, R109–R142 (2003).
6. S. S. P. Parkin, C. Kaiser, A. Panchula, P. M. Rice, B. Hughes, M. Samant, S. H. Yang, Giant tunnelling magnetoresistance at room temperature with MgO (100) tunnel barriers. *Nat. Mater.* **3**, 862–867 (2004).
7. S. Yuasa, T. Nagahama, A. Fukushima, Y. Suzuki, K. Ando, Giant room-temperature magnetoresistance in single-crystal Fe/MgO/Fe magnetic tunnel junctions. *Nat. Mater.* **3**, 868–871 (2004).
8. E. Y. Tsymbal, H. Kohlstedt, Tunneling across a ferroelectric. *Science* **313**, 181–183 (2006).
9. V. Garcia, S. Fusil, K. Bouzehouane, S. Enouz-Vedrenne, N. D. Mathur, A. Barthélémy, M. Bibes, Giant tunnel electroresistance for non-destructive readout of ferroelectric states. *Nature* **460**, 81–84 (2009).
10. V. Garcia, M. Bibes, Ferroelectric tunnel junctions for information storage and processing. *Nat. Commun.* **5**, 4289 (2014).
11. Z. Wen, D. Wu, Ferroelectric tunnel junctions: Modulations on the potential barrier. *Adv. Mater.* **27**, 1904123 (2019).
12. A. Chanthbouala, A. Crassous, V. Garcia, K. Bouzehouane, S. Fusil, X. Mova, J. Allibe, B. Dlubak, J. Grollier, S. Xavier, C. Deranlot, A. Moshar, R. Proksch, N. D. Mathur, M. Bibes, A. Barthélémy, Solid-state memories based on ferroelectric tunnel junctions. *Nat. Nanotechnol.* **7**, 101–104 (2012).
13. E. Y. Tsymbal, A. Gruverman, Ferroelectric tunnel junctions: Beyond the barrier. *Nat. Mater.* **12**, 602–604 (2013).
14. S. Boyn, S. Girod, V. Garcia, S. Fusil, S. Xavier, C. Deranlot, H. Yamada, C. Carretero, E. Jacquet, M. Bibes, A. Barthélémy, J. Grollier, High-performance ferroelectric memory based on fully patterned tunnel junctions. *Appl. Phys. Lett.* **104**, 052909 (2014).
15. R. Guo, Z. Wang, S. Zeng, K. Han, L. Huang, D. G. Scholm, T. Venkatesan, Ariando, J. S. Chen, Functional ferroelectric tunnel junctions on silicon. *Sci. Rep.* **5**, 12576 (2015).
16. C. B. Duke, *Tunnelling in Solids* (Academic Press, 1969).
17. V. Heine, Theory of surface states. *Phys. Rev.* **138**, A1689–A1696 (1965).
18. M. Y. Zhuravlev, R. F. Sabirianov, S. S. Jaswal, E. Y. Tsymbal, Giant electroresistance in ferroelectric tunnel junctions. *Phys. Rev. Lett.* **94**, 246802 (2005).
19. H. Kohlstedt, N. A. Pertsev, J. Rodriguez Contreras, R. Waser, Theoretical current-voltage characteristics of ferroelectric tunnel junctions. *Phys. Rev. B* **72**, 125341 (2005).
20. D. Pantel, M. Alexe, Electroresistance effects in ferroelectric tunnel barriers. *Phys. Rev. B* **82**, 134105 (2010).
21. Z. Wen, C. Li, D. Wu, A. Li, N. Ming, Ferroelectric-field-effect-enhanced electroresistance in metal/ferroelectric/semiconductor tunnel junctions. *Nat. Mater.* **12**, 617–621 (2013).
22. Y. W. Yin, J. D. Burton, Y. M. Kim, A. Y. Borisevich, S. J. Pennycook, S. M. Yang, T. W. Noh, A. Gruverman, X. G. Li, E. Y. Tsymbal, Q. Li, Enhanced tunnelling electroresistance effect due to a ferroelectrically induced phase transition at a magnetic complex oxide interface. *Nat. Mater.* **12**, 397–402 (2013).
23. H. Yamada, A. Tsurumaki-Fukuchi, M. Kobayashi, T. Nagai, Y. Toyosaki, H. Kumigashira, A. Sawa, Strong surface-termination effect on electroresistance in ferroelectric tunnel junctions. *Adv. Funct. Mater.* **25**, 2708–2714 (2015).
24. A. Quindeau, V. Borisov, I. Fina, S. Ostanin, E. Pippel, I. Mertig, D. Hesse, M. Alexe, Origin of tunnel electroresistance effect in $PbTiO_3$-based multiferroic tunnel junctions. *Phys. Rev. B* **92**, 035130 (2015).
25. J. P. Velev, J. D. Burton, M. Y. Zhuravlev, E. Y. Tsymbal, Predictive modelling of ferroelectric tunnel junctions. *npj Comp. Mater.* **2**, 16009 (2016).
26. H. Yamada, Y. Ogawa, Y. Ishii, H. Sato, M. Kawasaki, H. Akoh, Y. Tokura, Engineered interface of magnetic oxides. *Science* **305**, 646–648 (2004).
27. M. Huijben, Y. Liu, J. A. Boschker, V. Lauter, R. Egoavil, J. Verbeeck, S. G. E. te Velthuis, A. J. H. M. Rijnders, G. Koster, Enhanced local magnetization by interface engineering in perovskite-type correlated oxide heterostructures. *Adv. Mater.* **2**, 1400416 (2015).
28. E.-J. Guo, M. A. Roldan, T. Charlton, Z. Liao, Q. Zheng, H. Ambaye, A. Herklotz, Z. Gai, T. Z. Ward, H. N. Lee, M. R. Fitzsimmons, Removal of the magnetic dead layer by geometric design. *Adv. Funct. Mater.* **28**, 1800922 (2018).
29. S. Koohfar, A. B. Georgescu, A. N. Penn, J. M. LeBeau, E. Arenholz, D. P. Kumah, Confinement of magnetism in atomically thin $La_{0.7}Sr_{0.3}CrO_3/La_{0.7}Sr_{0.3}MnO_3$ heterostructures. *npj Quant. Mater.* **4**, 25 (2019).
30. D. Yi, P. Yu, Y.-C. Chen, H.-H. Lee, Q. He, Y.-H. Chu, R. Ramesh, Tailoring magnetoelectric coupling in $BiFeO_3/La_{0.7}Sr_{0.3}MnO_3$ heterostructure through the interface engineering. *Adv. Mater.* **31**, 1806335 (2019).
31. F. Ambriz-Vargas, G. Kolhatkar, R. Thomas, R. Nouar, A. Sarkissian, C. G. Yanez, M. A. Gauthier, A. Ruediger, Tunneling electroresistance effect in a $Pt/Hf_{0.5}Zr_{0.5}O_2/Pt$ structure. *Appl. Phys. Lett.* **110**, 093106 (2017).
32. N. F. Hinsche, M. Fechner, P. Bose, S. Ostanin, J. Henk, I. Mertig, P. Zahn, Strong influence of complex band structure on tunneling electroresistance: A combined model and ab initio study. *Phys. Rev. B* **82**, 214110 (2010).
33. D. Wortmann, S. Blügel, Influence of the electronic structure on tunneling through ferroelectric insulators: Application to $BaTiO_3$ and $PbTiO_3$. *Phys. Rev. B* **83**, 155114 (2011).
34. Y. Hikita, M. Nishikawa, T. Yajima, H. Y. Hwang, Termination control of the interface dipole in $La_{0.7}Sr_{0.3}MnO_3$/Nb:$SrTiO_3$ (001) Schottky junctions. *Phys. Rev. B* **79**, 073101 (2009).
35. R. Ramesh, D. G. Schlom, Creating emergent phenomena in oxide superlattices. *Nat. Rev. Mater.* **4**, 257–268 (2019).
36. S. Boyn, J. Grollier, G. Lecerf, B. Xu, N. Locatelli, S. Fusil, S. Girod, C. Carretero, K. Garcia, S. Xavier, J. Tomas, L. Bellaiche, M. Bibes, A. Barthélémy, S. Saïghi, V. Garcia, Learning through ferroelectric domain dynamics in solid-state synapses. *Nat. Commun.* **8**, 14736 (2017).
37. W. Huang, Y.-W. Fang, Y. Yin, B. Tian, W. Zhao, C. Hou, C. Ma, Q. Li, E. Y. Tsymbal, C.-G. Duan, X. Li, Solid-state synapse based on magnetoelectrically coupled Memristor. *ACS Appl. Mater. Interfaces* **10**, 5649–5656 (2018).
38. R. Berdan, T. Marukame, K. Ota, M. Yamaguchi, M. Saitoh, S. Fujii, J. Deguchi, Y. Nishi, Low-power linear computation using nonlinear ferroelectric tunnel junction memristors. *Nat. Electronics* **3**, 259–266 (2020).
39. W. J. Hu, W. J. Hu, Z. Wang, W. Yu, T. Wu, Optically controlled electroresistance and electrically controlled photovoltage in ferroelectric tunnel junctions. *Nat. Commun.* **7**, 10808 (2016).
40. Y. Su, X. Li, M. Zhu, J. Zhang, L. You, E. Y. Tsymbal, Van der Waals multiferroic tunnel junctions. *Nano Lett.* **21**, 175–181 (2021).
41. J. Wu, H.-Y. Chen, N. Yang, J. Cao, X. Yan, F. Liu, Q. Sun, X. Ling, J. Guo, H. Wang, High tunnelling electroresistance in a ferroelectric van der Waals heterojunction via giant barrier height modulation. *Nat. Electronics* **3**, 466–472 (2020).
42. M. Y. Zhuravlev, S. Maekawa, E. Y. Tsymbal, Effect of spin-dependent screening on tunneling electroresistance and tunneling magnetoresistance in multiferroic tunnel junctions. *Phys. Rev. B* **81**, 104419 (2010).
43. V. Garcia, M. Bibes, L. Bocher, S. Valencia, F. Kronast, A. Crassous, X. Moya, S. Enouz-Vedrenne, A. Gloter, D. Imhoff, C. Deranlot, N. D. Mathur, S. Fusil, K. Bouzehouane, A. Barthélémy, Ferroelectric control of spin polarization. *Science* **327**, 1106–1110 (2010).
44. D. Pantel, S. Goetze, D. Hesse, M. Alexe, Reversible electrical switching of spin polarization in multiferroic tunnel junctions. *Nat. Mater.* **11**, 289–293 (2012).
45. G. Sanchez-Santolino, J. Tornos, D. Hernandez-Martin, J. I. Beltran, C. Munuera, M. Cabero, A. Perez-Muñoz, J. Ricote, F. Mompean, M. Garcia-Hernandez, Z. Sefrioui, C. Leon, S. J. Pennycook, M. Carmen Muñoz, M. Varela, J. Santamaria, Resonant electron tunnelling assisted by charged domain walls in multiferroic tunnel junctions. *Nat. Nanotechnol.* **12**, 655–662 (2017).
46. A. T. Chen, Y. Wen, B. Fang, Y. Zhao, Q. Zhang, Y. Chang, P. Li, H. Wu, H. Huang, Y. Lu, Z. Zeng, J. Cai, X. Han, T. Wu, X.-X. Zhang, Y. Zhao, Giant nonvolatile manipulation of magnetoresistance in magnetic tunnel junctions by electric fields via magnetoelectric coupling. *Nat. Commun.* **10**, 243 (2019).
47. P. Giannozzi, S. Baroni, N. Bonini, M. Calandra, R. Car, C. Cavazzoni, D. Ceresoli, G. L. Chiarotti, M. Cococcioni, I. Dabo, A. D. Corso, S. de Gironcoli, S. Fabris, G. Fratesi, R. Gebauer, U. Gerstmann, C. Gougoussis, A. Kokalj, M. Lazzeri, L. Martin-Samos,

N. Marzari, F. Mauri, R. Mazzarello, S. Paolini, A. Pasquarello, L. Paulatto, C. Sbraccia, S. Scandolo, G. Sclauzero, A. P. Seitsonen, A. Smogunov, P. Umari, R. M. Wentzcovitch, Quantum ESPRESSO: A modular and open-source software project for quantum simulations of materials. *J. Phys. Condens. Matter.* **21**, 395502 (2009).
48. J. D. Burton, E. Y. Tsymbal, Prediction of electrically-induced magnetic reconstruction at the manganite/ferroelectric interface. *Phys. Rev. B* **80**, 174406 (2009).
49. A. A. Mostofi, J. R. Yates, G. Pizzi, Y. S. Lee, I. Souza, D. Vanderbilt, N. Marzari, An updated version of Wannier90: A tool for obtaining maximally-localised Wannier functions. *Comput. Phys. Commun.* **185**, 2309–2310 (2014).
50. A. Gruverman, D. Wu, H. Lu, Y. Wang, H. W. Jang, C. M. Folkman, M. Y. Zhuravlev, D. Felker, M. Rzchowski, C.-B. Eom, E. Y. Tsymbal, Tunneling electroresistance effect in ferroelectric tunnel junctions at the nanoscale. *Nano Lett.* **9**, 3539–3543 (2009).

Acknowledgments
Funding: The project was supported by Singapore Ministry of Education MOE2018-T2-2-043, A*STAR AMEIRG-A1983c0036, A*STAR IAF-ICP 11801E0036, and MOE Tier 1-R284000195114. J.S.C. is a member of the Singapore Spintronics Consortium (SG-SPIN). Research at the University of Nebraska-Lincoln was supported by the NSF through the Materials Research Science and Engineering Center (MRSEC) (NSF grant no. DMR-1420645). Computations were performed at the University of Nebraska Holland Computing Center. **Author contributions:** R.G. and J.C. conceived the project. E.Y.T. and L.T. developed the theoretical concept. R.G. fabricated the FTJ devices, measured PFM, and carried out the electrical measurements. L.T., M.L., and E.Y.T. performed the DFT calculations and data analysis. Z.L., X.C., and H.T. carried out the TEM characterization. R.G., E.Y.T., and J.C. wrote the manuscript. All the authors participated in discussions of the results and/or contributed to the amendment of the manuscript. J.C. and E.Y.T. supervised the whole project. **Competing interests:** The authors declare that they have no competing interests. **Data and materials availability:** All data needed to evaluate the conclusions in the paper are present in the paper and/or the Supplementary Materials. Additional data related to this paper may be requested from the authors.

Submitted 4 October 2020
Accepted 5 February 2021
Published 24 March 2021
10.1126/sciadv.abf1033

Citation: R. Guo, L. Tao, M. Li, Z. Liu, W. Lin, G. Zhou, X. Chen, L. Liu, X. Yan, H. Tian, E. Y. Tsymbal, J. Chen, Interface-engineered electron and hole tunneling. *Sci. Adv.* **7**, eabf1033 (2021).